Light-Activated Artificial CO 2 -Reductase: Structure and Activity

Raphaël J. Labidi, Bruno Faivre, Philippe Carpentier, Julien Pérard, Philipp Gotico, Yun Li, Mohamed Atta, Marc Fontecave

Light-activated artificial CO$_2$-reductase: structure and activity.

Raphaël J. Labidi[1], Bruno Faivre[1], Philippe Carpentier[2,4], Julien Perard[2], Philipp Gotico[3], Yun Li[1], Mohamed Atta[2] and Marc Fontecave[1*]

[1]Laboratoire de Chimie des Processus Biologiques, UMR 8229, Collège de France/CNRS/Sorbonne Université, 11, place Marcellin-Berthelot, Paris 75005, France

[2]Laboratoire de Chimie et Biologie des Métaux, DRF/IRIG/CBM, UMR 5249 CEA/CNRS/UGA, CEA/Grenoble, 17, rue des Martyrs, Grenoble 38000, France.

[3]Laboratoire des Mécanismes Fondamentaux de la Bioénergétique, DRF/JOLIOT/SB2SM, UMR 9198 CEA/CNRS/I2BC, Gif Sur Yvette 91191, France.

[4]European Synchrotron Radiation Facility, Grenoble 38000, France.

*To whom correspondence should be addressed.

Email: marc.fontecave@college-de-france.fr;

Abstract

Light-dependent reduction of carbon dioxide (CO_2) into value-added products can be catalyzed by a variety of molecular complexes. Here we report a rare example of a structurally characterized artificial enzyme, resulting from the combination of a heme binding protein, heme oxygenase, with cobalt-protoporphyrin IX, with good activity for photoreduction of CO_2 to carbon monoxide (CO). Using a copper-based photosensitizer, thus making the photosystem free of noble metals, a large turnover frequency value of ~ 616 h^{-1}, a turnover value of ~ 589, after 3 h reaction, and a CO vs H_2 selectivity of 72 % were obtained, establishing a record among previously reported artificial CO_2 reductases. Thorough photophysical studies allowed tracking reaction intermediates and provided insights into the reaction mechanism. Thanks to a high-resolution crystal structure of the artificial enzyme, both in the absence and in the presence of the protein-bound CO_2 substrate, a rational site-directed mutagenesis approach was used to study the effect of some modifications of the active site on the activity.

Introduction.

Electro- and/or photo-reduction of carbon dioxide (CO_2) into energy-dense chemicals of economic value, *e.g.* carbon monoxide and formic acid as primary targets, is emerging as a key strategy for valorizing this carbon source in excess in our atmosphere.[1] It can also serve as a process for storing renewable and intermittent energies, such as solar energy, into chemical energy (the energy in chemical bonds). Development of this technology obviously requests the discovery of cheap, stable, efficient and selective catalysts and a better fundamental understanding of multi-electronic and multi-protonic mechanisms associated with CO_2 activation.[2] Selectivity is a specifically challenging issue in the case of CO_2 reduction, since different products can form at quite close redox potentials and since proton reduction competes with CO_2 reduction.

Heterogeneous and homogeneous catalysts have been extensively explored during the last 20 years.[3-5] In contrast, the enzymology approach has been underexplored even though fascinating natural CO_2 reduction enzymes (CO_2Rases), such as carbon monoxide dehydrogenases (CODH) and formate dehydrogenases (FDH), catalyzing reversible CO_2 reduction to CO and HCOOH, respectively, with very high efficiency and selectivity, have been discovered.[6-7] Unfortunately, these enzymes are very difficult to prepare in pure form as their production depends on complex maturation machineries and they are extremely sensitive to oxygen. Therefore, they seem quite inappropriate for biotechnological development so far. We thus here consider a novel approach, aiming at designing, preparing, and characterizing semisynthetic artificial CO_2 reductases (named ACRs hereafter). Artificial enzymology currently enjoys increasing interest as a way to expand the repertoire of enzymes, via anchoring a synthetic molecular catalyst into a protein host, not necessarily an enzyme, through covalent or non-covalent interactions.[8] This strategy combines attractive features of both molecular and enzymatic catalysis. The protein environment might give the synthetic catalysts a new dimension, favoring catalysis: greater water solubility, greater activity, selectivity, and greater stability (by isolating the catalyst, the protein prevents it from bimolecular deactivating processes). Furthermore, such hybrid systems may rival natural CO_2Rases with the following specific benefits: (i) much easier preparation; (ii) tunability via both site-directed mutagenesis of the protein (in order to manipulate primary and secondary coordination sphere interacting with the catalyst, the substrate, or intermediates) and synthetic variations of the catalyst (ligand and metal); (iii) greater stability. Such an artificial

3

enzymology strategy has been extensively used for a variety of hydrogenation, C-C bond formation, and hydration and oxidation reactions.[8]

In contrast, there are, to our knowledge, only very few examples of ACRs reported so far (Table S1). These are mainly light-driven photosystems achieving CO_2 photo-reduction in the presence of a photosensitizer and a sacrificial electron donor, with the exception of an artificial iron-sulfur protein, based on the well-known biotin-streptavidin approach, recently reported for its catalytic activity for CO_2 reduction to hydrocarbons by a strong Eu-based chemical reducing agent, in the absence of light.[9] In a first example, both Lehn's catalyst, [Re(bpy)(CO)$_3$]Cl, and a Ru-based photosensitizer were covalently attached to a β-helical protein nanotube, and the resulting assembly was poorly active (TOF ~ 1 h^{-1}) during photocatalytic reduction of CO_2 in a 1:1 water:DMF solvent using 1-benzyl-1,4-dihydronicotinamide as a sacrificial reducing agent.[10] In a second system, [Ni(cyclam], a well-known molecular catalyst for CO_2 reduction to CO, was attached to azurin, a copper protein, through a histidine-nickel coordination bond. This hybrid system catalyzes the photoreduction of CO_2 to CO in water, in the presence of ascorbate as the sacrificial reducing agent and a Ru-based photosensitizer, however with very low activity (TON = 4.6 after 2 hours reaction).[11-12] As another example, a photosensitizing protein became photoactive for CO_2 reduction to carbon monoxide (CO) or formic acid after attachment of either a Ni(terpyridine) complex or iron-sulfur clusters, respectively, here also with limited reaction rates (TON = 35-85 after 12 hours).[13-14] Finally, during the course of this work, an intriguing class of metal-free proteins, selected for having a well-defined CO_2 binding pocket, was reported to display a catalytic activity for CO_2 photoreduction (TON = 143 after 3 hours reaction for phenolic acid decarboxylase).[15]

Here we demonstrate that the combination of a heme binding protein, heme oxygenase, with cobalt-protoporphyrin IX results in a highly active and selective ACR, named HmuO-Co^{III} in the following. Also during the course of this investigation, Y. Deng and collaborators reported an ACR based on myoglobin loaded with the same Co-protoporphyrin IX cofactor.[16] A Co-porphyrin has also been covalently attached to a protein providing it with a weak activity for CO_2 photoreduction.[17] Co-porphyrins have been selected as they are well-known as catalysts for CO_2 photo- and electro-reduction to CO in organic and aqueous solvents, either in homogeneous[18-20] or heterogeneous[21-24] systems. Since our best results were obtained with a water-soluble copper-based photosensitizer,[20] we report the first fully noble metal free light-assisted CO_2 reduction catalyzed by an ACR. Finally, the determination of the first high-

4

resolution crystal structure of HmuO-Co^{III}, both in the absence and in the presence of the protein-bound CO_2 substrate, provides a rare three-dimensional structure of an ACR, and allowed studying the ACR-CO_2 interaction at the molecular level and preliminary rational tuning of its reactivity via mutagenesis. Photophysical studies further allowed tracking reaction intermediates and provided insights into the reaction mechanism.

Results.

Preparation and characterization of HmuO-Co^{III}. The heterologous overexpression of HmuO from *Corynebacterium diphtheriae* in *Escherichia coli* resulted in a large production of the protein mainly in the *apo*-form. This behavior is frequently observed for hemoproteins and has previously been described as an unequal rate of *apo*-protein production and heme biosynthesis under overexpression conditions.[25-26] Homogeneous *apo*-HmuO was prepared and purified as described in the supplementary information (SI) section, analyzed by SDS-PAGE and evaluated to be >95% pure (Figure S1-A). The purified *apo*-HmuO was reconstituted with cobalt-protoporphyrin IX to afford HmuO-Co^{III} as described in the SI section. After desalting column, SEC-MALLS-RI analysis revealed one main elution peak with a molecular weight around 24.1 kDa corresponding to a monomer (Figure S1-B). Metal analysis of the reconstituted HmuO-Co^{III}, by Inductively Coupled Plasma Optical Emission spectrometry (ICP-OES), showed the presence of ~ 1 Co atom bound to one monomer. The UV-Visible absorption spectrum of the reconstituted protein displayed, in addition to the band at 280 nm corresponding to protein absorption, three bands characteristic for the presence of protein-bound Co-protoporphyrin IX: the Soret band at 420 nm and the α and β bands at 530 and 564 nm, respectively (Figure 1-A). This electronic absorption spectrum is similar to those published for myoglobin loaded with the same Co-protoporphyrin IX cofactor.[16, 27-28] Altogether, these data show that the *apo*-HmuO was correctly loaded with the metalloporphyrinic cofactor. *Apo*-HmuO was also reconstituted with Mn-, Cr- and Zn-protoporphyrin IX. The pure preparations were characterized by ICP-OES and by light absorption spectroscopy. Metal quantification led to 0.63 (Mn), 0.93 (Cr) and 0.69 (Zn) per monomer. UV-Visible spectra were comparable to those of myoglobin loaded with the same metal ions (Figure S2).[29-31]

Crystal structure of the HmuO-Co^{III}. We determined the X-ray crystal structure of HmuO-Co^{III}, to highlight possible differences with that previously reported for HmuO-Fe^{III} [32] and more specifically to obtain structural information regarding the Co^{III}-porphyrin active site.

Optimization of the crystallization conditions is described in the SI section. Purple well-diffracting crystals (typically 30 x 30 x 300 μm^3) were obtained using the best crystallization condition (12-16% PEG 1000 and 0.1M citric acid at pH 3.5) (Figure S3). We used the helical data-collection strategy to record a series of 7 identical datasets but at increasing X-ray doses from 119 kGy to 2.44 MGy, in order to evaluate radiation effects on the protein (see SI section and Figure S4). The sequence of difference density maps (Fo^i-Fo^1) calculated between the ith data-set ("i" ranging from 2 to 7) and the first one (of lower dose) revealed the dose-dependent effects of X-ray radiation on the metal cofactor and its environment. First, it shows that the Co-porphyrin-coordinated water molecule together with the water molecules in the distal pocket move slightly away from the Co ion upon increasing X-ray dose. His20, the second axial ligand in the proximal pocket, is also displaced from the Co ion. We observed that the porphyrin ring remained unaffected even at the highest X-ray dose. These structural changes are identical to those observed in the HmuO-Fe during the transition from ferric to ferrous state.[32] This opens the possibility that the Co-porphyrin cofactor got reduced by photoelectrons during exposure to high doses of X-rays, leading to a weakening of Co-OH_2 and Co-His20 bonds. The dataset with the lowest dose (119 kGy) was thus used to solve the HmuO-Co^{III} reference structure with the highest resolution and restricted X-ray induced structural changes. A summary of diffraction data collection and analysis, and structure refinement statistics are listed in the supplementary information Table S2. The structure of HmuO-Co^{III} could thus be obtained with a remarkable resolution (1.15 Å).

The HmuO-Co^{III} fold is a compact alpha-helix domain, as shown in Figure 2A and Figure S5, is essentially identical to that of the wild type HmuO-Fe^{III} (pdb code 1IW0) (Cα r.m.s.d. of 0.34 Å).[32] Thus, the chemical environment of the metalloporphyrin cofactor is the same as in the HmuO-Fe^{III} structure.[32] First, the Co-protoporphyrin IX is perfectly embedded into the HmuO active site pocket, housed between the proximal "a" and the distal "h" helices (in magenta and yellow respectively in Figure 2-A), in exactly the same manner as the heme substrate in the native structure. In particular, the cobalt atom is liganded by the proximal His20 and a distal water molecule, in line with a Co^{III} state. This state was further confirmed by *in crystallo* optical spectroscopy icOS,[33] the UV-Vis absorption spectrum of crystals displaying 3 bands peaking at 425, 534 and 566 nm, corresponding to the γ-Soret, α and β absorption bands characteristic for a Co^{III}-protoporphyrin IX, with His/H_2O axial ligands (Figure 1-B). Second, the protoporphyrin IX is oriented in this pocket by its propionate groups exposed at the protein surface and forming strong ionic/hydrogen bond interactions

either directly or via a water molecule with Lys13, Tyr130 and Arg177 for one of the groups and with Glu24 and Lys13 for the other one, and thus closing the active site pocket (Figure S6). Third, the protoporphyrin IX macrocycle is embedded inside the active site owing to important hydrophobic/Van der Waals contacts with residues Ala23, Leu33, Met29, Val131, Gly135, Ser138, Gly139, Ile143, Phe201, Asn204, and Phe208 that line up the pocket (Figure S6). Fourth, as in the HmuO-Fe^{III} structure,[32] an internal distal cavity (volume of 55 Å^3 calculated by BetaCavityWeb using a sphere probe of 1.4 Å radius[34]) is filled with a cluster of 14 water molecules, including the water ligand bound to the Co^{III} ion, stabilized by a complex network of H-bonding interactions, to which hydrophilic residues, Asp136 and Arg132, as well as Tyr161 participate (Figures 2-B and S7).[35] The water molecules in this cavity extend their H-bonding network to the surface of HmuO, so that the H$_2$O ligand is connected to Asp86 at the surface of the protein and thus accessible to the solvent. The water-filled cavity is limited with predominantly hydrophobic residues (Met29, Phe208, Val207, and Leu45) on one side and two glycines, Gly 139 and Gly140, providing some flexibility (Figure S8-A). The water cavity is an interesting feature of the structure as it provides a proton transfer pathway from the solvent to the active site, which is key for O$_2$ activation during heme oxidation,[36] the biological function of HmuO-Fe^{III}, but also for CO$_2$ activation. It was also proposed to be the target for binding inhibitors or small molecules that may modify the HmuO oxygenase catalytic process.[36]

Three-dimensional structure of HmuO-Co^{III} in complex with CO$_2$. To identify the pockets that can host CO$_2$ molecules within HmuO-Co^{III}, we used the facility of the High Pressure (HP) Macromolecular Crystallography Laboratory (HPMX, ESRF, Grenoble, France).[37-38] CO$_2$ molecules were introduced by soaking crystals in a pure CO$_2$ pressurized atmosphere. In practice, to produce these HmuO-Co^{III}-CO$_2$ derivatives, crystals were pressurized and flash-cooled within 58 bar of CO$_2$ using a specially designed pressure cell.[38] The diffraction data collection, phase determination, and structure refinement statistics of the best derivative crystal are described in the SI section (Table S2). Despite the pressurization, the overall structure of the HmuO-Co^{III}-CO$_2$ derivative is identical to that of the native enzyme. However, a careful analysis of the electron density map revealed the presence of an additional strong elongated peak at the vicinity of the cobalt-protoporphyrin IX cofactor, accommodated within the reorganized distal cavity (see the omit electron density map in Figure S9-A). Several possible models were assessed, in which a single water (H$_2$O), a diatomic (O$_2$ or CO) and a tri-atomic (CO$_2$) molecule were successively positioned and refined to explain this

residual density (Figure S9-B to S9-E). Clearly, a triatomic molecule, most likely CO_2, best models the observed electron density, as demonstrated by the residual map (Fo-Fc, contoured at 3.5σ in Figures S9-A to S9-E), which disappears only when a CO_2 molecule is ideally placed, while all other models failed to explain the electron density. Furthermore, by calculating the inner distal cavity using a probe with a larger radius of 2 Å (BetaCavityWeb,[34] green mesh in Figure S8-B) to accommodate larger ligands such as CO_2, the possible CO_2 binding sites are indeed restricted around the proposed position. It is worth adding that this precise site has already been described as capable of accommodating ligands such as a dithiothreitol molecule (pdb 3I8R).[36] The CO_2 molecule is positioned close to the Co ion, with a Co-O and Co-C distances of 3.3 and 3.8 Å respectively, and confined within the distal water-filled cavity now containing only six water molecules (Figures 2-C and 2-D). In the HmuO-Co[III]-CO_2 derivative, the Co ion is five-coordinated involving only the proximal His20 as axial ligand, since the water ligand is no longer present in this case, leaving *de facto* a free coordination site for the possible binding and activation of a CO_2 molecule (Figure 2-D). This figure details the bonding network extended from Co ion to Asp86 at the surface of the protein. Interestingly one oxygen atom of CO_2 is H-bonded to a water molecule, which likely favors C-O bond heterolytic cleavage during CO_2 reduction.

To get further evidence of the presence of CO_2 molecules in the HmuO-Co[III]-CO_2 crystal, we used *in crystallo* Raman spectroscopy at the iCOS laboratory (ESRF, Grenoble)[33, 39] (SI section). Figure 3 shows the Raman spectra measured on: (a) a native crystal of HmuO-Co[III] without cryo-protection, (b) a cryo-protected native crystal of HmuO-Co[III], and (c) the cryo-protected crystal of HmuO-Co[III]-CO_2. Although cryo-protection is unnecessary for Raman spectroscopy, the addition of 25% of glycerol was required for the crystals on which both diffraction and Raman data were collected. Spectrum (a) allows attributing typical vibrational frequencies of HmuO amino acid residues on the basis of databases well-established in the literature[40]: the band (1) at 760 cm^{-1} corresponds to tryptophan vibrations, (2) the one at 1003 cm^{-1} to phenylalanine vibrations, and (3) those between 1600 and 1700 cm^{-1} to the amide I bands. The comparison between spectra (a) at (b) allows deducing the typical Raman bands due to glycerol vibrations (4, 5, and 6) peaking at 850, 1050, and 1470 cm^{-1} respectively. Conclusively, comparison of spectra (a), (b), and (c) reveals two prominent additional bands peaking at 1280 and 1385 cm^{-1} in the spectrum of the HmuO-Co[III]-CO_2 derivative. This doublet corresponds neither to protein nor to glycerol vibrations, but instead to the Fermi dyad of the extremely Raman-active CO_2 stretching vibrations, the values of which are well documented in the literature.[41] This confirmed the presence of CO_2 in the crystal and

supported the assignment of the elongated electron density inside the HmuO-Co[III] distal pocket as a CO_2 molecule (Figure 2C).

Photoreduction of CO_2 catalyzed by HmuO-Co[III]. Light-dependent CO_2 reduction catalyzed by HmuO-Co[III] was evaluated at 20 °C under anaerobic conditions using a water-soluble copper-diimine-diphosphine complex, named Cu-PS in the following, (Na_4[Cu(L1)(L2)]BF_4, L_1=2,9-dimethyl-4,7-diphenyl-1,10-phenanthroline-5,6-disulfonate, L_2=9,9-dimethyl-4,5-bis(diphenylphosphino)xanthene-2,7-disulfonate), as the photosensitizer and sodium L-ascorbate as the sacrificial electron donor agent. Cu-PS was synthesized as previously described[20] and its UV-Visible and ^{1}H-NMR spectra are shown in Figure S10-A and B respectively. Considering that the Co-porphyrin is close to the surface of the protein, we anticipated that Cu-PS in solution would be functional for electron transfer, in spite of its large size. The reaction was carried out in an aqueous solution of 100 mM phosphate buffer, saturated with CO_2 (pH 6.65), under irradiation with visible light using a Xe lamp ($\lambda > 400$ nm). At time intervals, the headspace was monitored by gas chromatography and the liquid phase by ion-exchange chromatography and NMR spectroscopy. This demonstrated that the system was functional for CO_2 reduction as it produced CO as the major product, together with H_2, while no CO_2-derived liquid product, including formate monitored by ion-exchange chromatography, could be detected. In control experiments, no product could be observed when Cu-PS or ascorbate was omitted from the reaction mixture (Figure S11-S14). No product was formed either when the reaction was carried out in the dark. When HmuO-Co[III] was absent, tiny amounts of H_2 and no CO could be detected (Figure S15-S16). This demonstrated the strict requirement for the complete system and notably the catalytic role of HmuO-Co[III].

The photocatalytic activity of the HmuO-Co[III] dependent system was optimized in terms of CO production via a series of kinetic experiments in which the concentrations of each component of the system were varied: the catalyst (0 - 20 μM), the photosensitizer (0 - 1.25 mM) and sodium L-ascorbate (0 - 0.3 M). Reaction products were monitored during 4 hours, as their production reached a plateau after about 3 hours. The reaction was characterized by the three following parameters: (i) the amount of CO and H_2 produced after 3 hours; (ii) the initial maximal production rate or Turnover Frequency (TOF°); (iii) the selectivity of the photosystem for CO_2 reduction *vs* proton reduction (Sel_{CO_2} (%) $= TOF_{CO}°/ [TOF_{CO}°+ TOF_{H_2}°]$). The data of these investigations are shown in Figures S11-S17.

Figures S11-S12 show an increased production of CO and H_2, using 5 µM of HmuO-Co^{III}, upon increasing Cu-PS concentration up to 0.75 - 1 mM, at which the total amount of products and the initial reaction rate were maximal. One should note that the time at which the plateau was reached decreased with decreased concentration of Cu-PS, suggesting that the system was limited by the stability of Cu-PS. Thus, a Cu-PS concentration of 1 mM was used for the following experiments. In Figure S18-A, we show that using the prototypical organometallic photosensitizer, [Ru(bipyridine)$_3$]Cl$_2$, at the same concentration of 1 mM, resulted in a lower production of CO, levelling off after 4 hours, together with a sustained production of H_2, so that Sel$_{CO}$ was < 50% and decreased with time. This is likely to be due to the well-known degradation of this photosensitizer, during irradiation, giving species highly catalytic for proton reduction, as can be seen from an experiment in the absence of catalyst (Figure S18-B).[42] No CO and H_2 production could be observed using HmuO-M preparations, with M = Cr^{III}, Zn^{II}, Mn^{III} under these conditions.

Figure S15-S16 show, as expected, increased production of CO and H_2 and increased initial rates as a function of HmuO-Co^{III} concentration, varying from 0 to 20 µM. However, this translated into a trend with TONs (TurnOver Numbers after 3 hours reaction) and initial TOF°s (TurnOver Frequencies in h^{-1}) decreasing as a function of HmuO-Co^{III} concentration (Figure 4). This is a typical behavior as the consequence of an increased catalyst/photosensitizer ratio, which results into a decreased amount of reducing equivalents that each molecule of catalyst can receive during a given period of time. Furthermore, no effect of protein concentration on the time at which the reaction stops could be observed (Figures S15-S16). Figures S13-S14 show that the optimal ascorbate concentration was 0.1 M, a value selected for the optimal photosystem. Interestingly, within such a broad range of component concentrations, the selectivity of the photosystem for CO_2 reduction *vs* proton reduction (Sel$_{CO}$) was relatively constant between 70 and 80 % (Figure S17).

In Figure 4-C, we report the kinetics for the most efficient system in terms of TONs and TOF°s, using 0.5 µM Hmu-Co^{III}, 1 mM Cu-PS and 0.1 M sodium L-ascorbate in 0.5 M phosphate buffer, pH 6.65. Under these conditions, a TOF° value of ~ 616 h^{-1}, a TON value of ~ 589 after 3 h reaction, and a selectivity of 72 % were obtained. The quantum yield for CO production was determined at 0.55 %, under these conditions and upon irradiation at 400 nm, following the methodology described in the experimental section.

As generally observed the studied photosystem degraded during irradiation and stopped being functional after about 3 hours reaction. In Figure S19, we show that the system could not be repaired by a fresh addition of either Cu-PS or HmuO-Co^{III} or ascorbate after 2.5 hours

reaction. However, CO and H_2 production resumed after addition of both Cu-PS and HmuO-Co^{III} together (Figure S20). This indicated that both the catalyst and the photosensitizer were deactivated during the reaction.

Myoglobin was also loaded with Co-protoporphyrin IX, as described.[16] The Myo-Co^{III} protein was shown to contain 0.85 Co per monomer and its light absorption spectrum identical to that previously reported[16]. Under optimal conditions, this catalyst gave a TON_{CO} of 373, as compared to 506 for HmuO-Co^{III} and a TON_{H2} of 184, as compared to 201, after 1.5 h reaction.

Site-directed mutagenesis effects on CO_2 photoreduction catalyzed by HmuO-Co^{III}. Based on the structure of HmuO-Co^{III} in complex with CO_2, we selected amino-acids in the vicinity of the Co cofactor and the molecule of CO_2 in the distal cavity for site-directed mutagenesis, with the objective of modulating the activity of the artificial enzyme (Figure S21). Specifically, the first coordination sphere was modified via mutation of His20 into Cys20 and Tyr20, two alternative residues that can coordinate a metal ion as in cytochromes P450 (*e.g.* pdb-2CPP)[43] and in catalases (*e.g.* pdb-2CAG),[44] respectively. Furthermore, the close environment of CO_2, constituted by Gly139 and Ile143, was modified via the single Gly139Ala, Gly139His, and Ile143Lys mutations. Gly139Ala and Ile143Lys mutations were selected as to modify the hydrophobicity of the CO_2 environment while Gly139His mutant served to introduce a Histidine-based H-bond interaction with CO_2 potentially favoring C-O bond dissociation. Figure S21 shows the model structures of the mutants based on HmuO-Co^{III} structure with CO_2 in the position obtained after pressurization, which justify the choice of mutations. All mutant proteins were purified and reconstituted with Co-PPIX. They were characterized by ICP-OES (giving a Co content per monomer of 1.0, 0.7, 0.7, 1.1, and 0.9 for His20Cys, His20Tyr, Gly139Ala, Ile143Lys, and Gly139His, respectively) and by UV-Visible spectroscopy (Figure S22). Interestingly, some mutants, His20Cys, Gly139Ala, and Ile143Lys could be crystallized and their structure determined with a sufficient resolution (2.30Å, 1.40Å, and 2.85Å, respectively) to assess the effects of mutations (Figure S23-A, C, and E). Mutations had no effect on the overall structure. In Figures S23-B, D, and F, models of the structures of the mutants in complex with CO_2 are provided, in which the CO_2 is positioned as in the structure of HmuO-Co^{III}-CO_2. Figure S23 provides the following outcomes: (i) the extra methyl group in Gly139Ala has no effect on the distal cavity and comes close to the CO_2 binding site, as anticipated (Figure S23-A and B); (ii) as Cys20 side-chain is shorter than that of His20, the S atom is not a ligand of the Co ion in the His20Cys

11

mutant and, instead, Co is ligated by a proximal water molecule bridging S and Co (Figure S23-C and D); (iii) in the Ile143Lys mutant, the new side chain occupies a larger space in the distal cavity but with minor effect on the water molecules and the amine group comes close to the CO_2 binding site, as anticipated (Figure S23-E and F).

The results regarding mutant activity are given in Figures S24-S25 and summarized in Figure 4-D, in which $TOF_{CO}°$ and selectivity values are compared to those of the wild-type protein. They show that mutations had only small effects on these parameters. In all cases, the selectivity was slightly degraded by the mutations. It turned out that only Gly139Ala displayed a larger CO_2 reduction activity, while changing Gly139 to histidine had no effect, suggesting a positive effect of increased hydrophobicity in the vicinity of the CO_2 binding site. Changing the His ligand into Cys or Tyr had almost no effect, likely related to the weak interaction between the cobalt ion and the axial ligand under reducing conditions. Finally, the most degraded activity was observed with the Ile143Lys mutant, which was twice less active than the Gly139Ala mutant, the most active artificial system in this study. It is possible that Lys introduces some steric hindrance that limits CO_2 binding.

Probing the photocatalytic mechanism. Nanosecond transient absorption spectroscopy and *in situ* spectroscopy were used to track relevant chemical intermediates during catalysis. Exciting the Cu-PS photosensitizer at 420 nm resulted in an emission at 552 nm (Figure S26-A), with an excited state lifetime of 20 μs (Figure S26-C)[20]. The excited state Cu-PS* is characterized by a positive absorption band at 550 nm (Figure S26-B), attributed to the triplet metal-to-ligand charge transfer (^{3}MLCT). Emission quenching experiments were then performed to determine the quenching pathway of the system. Reductive quenching occurs when the excited state Cu-PS* is quenched by the electron donor (*i.e.,* ascorbate) to give the one-electron reduced species Cu-PS$^{•-}$ while oxidative quenching occurs when the excited state Cu-PS* is quenched by the catalyst acting as the electron acceptor to give the oxidized Cu-PS$^{•+}$ and the reduced catalyst. We experimentally determined a dynamic reductive quenching rate of $k_{q,asc} = 2.2 \times 10^7$ M^{-1}s^{-1} (Figure S27) and oxidative quenching constant of $k_{q,cat} = 1.8 \times 10^9$ M^{-1}s^{-1} (Figure S28), all within a diffusion limited regime. Using the optimized photocatalytic conditions (concentration of 0.5 μM HmuO-Co^{III} and 100 mM ascorbate), the reductive quenching pathway is dominant with a rate of $k_{q,asc}$[Asc] $= 2.2 \times 10^6$ s^{-1} , three orders of magnitude faster than the oxidative quenching pathway (rate of $k_{q,cat}$[Cat] $= 9.2 \times 10^3$ s^{-1}).

Upon reductive quenching of the Cu-PS* excited state, a one-electron reduced species Cu-PS$^{\bullet-}$ is formed, characterized by an absorption at 450 nm, with a lifetime of 595 μs (Figure S29). This feature is consistent with a previously reported spectroelectrochemical study of the same water-soluble photosensitizer.[20] Upon addition of the HmuO-Co^{III} catalyst, we observed a decay of this 450 nm-absorbing species to form a long-lived new species characterized by a bleaching at 400 nm and a positive absorption at 425 nm (Figure 5-A). This was not consistent with the reduction of Co(III) to Co(II), as previously observed for a similarly embedded Co-protoporhyrin IX[45] characterized by a bleaching at 425 nm and absorption at 400 nm. Suspecting an effect of the probe light, we spectrally followed the changes in the solution without laser excitation. As can be seen in Figure S30, we clearly observed that the probe light was responsible by itself for the accumulation of Co(II) species, characterized by a bleaching at 423 nm and a positive absorption at 396 nm. This probe-induced background thus caused the observed artifact, since the starting state would already contain Co(II) species. Nevertheless, the decay kinetics at 450 nm and 400 nm at increasing catalyst concentrations (Figure S31) were sufficient to estimate the rate of electron transfer for the reduction of Co(III) to Co(II) by the reductant Cu-PS$^{\bullet-}$ to be $k_{ET} = 1.0 \times 10^8$ M^{-1}s^{-1}.

We performed *in situ* spectroscopy on a CO$_2$-saturated solution of Cu-PS and HmuO-Co^{III} to get insight into relevant intermediates involved during photocatalysis. In Figure 5-B the immediate reduction of Co(III) to Co(II) happened within 30 seconds, characterized by the bleaching at 422 nm and a new absorption at 397 nm. This is one of the rare *in situ* spectroscopic studies that shows the successful photo-reduction of Co protoporphyrin embedded in artificial proteins, as most have relied on chemical reduction with sodium dithionite.[17, 45] It is important to underline that even though CO$_2$ was found near the Co(III) metal center in the crystal structure of HmuO-Co^{III}, this did not influence the spectral characteristic of neither Co(III) nor Co(II). This suggests that neither of these species are catalytically active to capture the CO$_2$ substrate. With further irradiation of the solution, we see a slow photodegradation of the Cu photosensitizer, characterized by the bleaching of its ground state spectrum (Figure 5-B). As this time scale is that of catalysis, we can infer that the Co(II) species is the cofactor steady state during catalysis and that the reduction of Co(II) to a formal Co(I) state is rate limiting, the latter state being the catalytically active species, as previously reported for similar Co macrocylic systems.[46-47] All these photophysical results help establish a proposed photocatalytic cycle (Figure 6) for the photo-induced CO$_2$ reduction activity of an artificial CO reductase based on HmuO-Co^{III}.

Discussion

While artificial hydrogenases have been extensively studied for photoreduction of protons into H_2,[8, 48] the field of artificial enzymology for CO_2 photoreduction has been much less explored. In Table S1 we provide a complete list of previously reported ACRs which proved catalytically active during light-induced CO_2 reduction to CO or formic acid. The system we report here, based on the artificial HmuO-Co[III] enzyme, differs from the listed systems as it uses a Cu-based photosensitizer, in place of benzophenone and the usual $[Ru(bpy)_3]Cl_2$ complex. With a maximal $TOF_{CO}°$ of 616 h^{-1} and a TON of 589 after 3h reaction, it is greatly superior to most previously reported systems and comparable to the Myo-Co[III] system. Furthermore, it is unique as the artificial enzyme component could be exquisitely characterized thanks to a high-resolution crystal structure in complex with the CO_2 substrate, providing clear insights into the structure of the active site and the appropriate information for a rational design of site-directed mutants.

Some previously reported ACR systems have also used a Co-porphyrin as the active catalytic component within different host proteins, cytochrome b562, αRep, or myoglobin (Table S1), as we did here. This is due to the fact that Co-porphyrins are good catalysts for CO_2 photoreduction and that hemoproteins have good affinity for Co-protoporphyrin IX. The mechanism has been well established: it involves reduction of Co(III) to Co(I), which then binds and activates CO_2, and subsequent electron transfer to CO_2 results in proton-assisted C-O bond cleavage generating CO.[16-17, 49] Thanks to detailed time-resolved photophysical studies, allowing tracking catalytic intermediates, we have established that the same mechanism is likely to operate here.

Interestingly, the choice of the host protein is very critical since, for the same molecular catalyst, namely Co-protoporphyrin IX, great differences in terms of catalytic activity were obtained from one system to another, as shown in Table S1, thus reflecting the great sensitivity of this catalyst to the protein environment. On this basis, we expected a larger effect of mutations on the catalytic activity of HmuO-Co[III], but only a factor of 2 was observed, in terms of initial catalytic rate, between the most and least active mutant. This is possibly due to the fact that the natural water molecules network provides an efficient mechanism of CO_2 activation and that a single mutation is insufficient for changing the CO_2 environment and modifying activation barriers. It suggests that more complex mutagenesis approaches, with multiple mutations, should be explored.

A special discussion should concern the related ACR, Myo-Co[III], derived from the combination of myoglobin and Co-protoporphyrin IX, which was reported during the course

of our study.[16] Also in that case, single mutation of the distal site had limited effects on the activity, with a factor of 2 between the unmodified protein and the most active mutant. Comparison with HmuO-Co^{III} is difficult since the conditions used were significantly different, in particular with respect to the concentration of the enzyme and the use of [Ru(bpy)$_3$]Cl$_2$ as the photosensitizer, which perturbed the system significantly: selectivity varied extensively upon modification of the catalyst concentration and formate was also formed as a consequence of degradation of [Ru(bpy)$_3$]Cl$_2$. As a consequence, using comparable concentrations of ACR, 0.5 - 1.3 μM, HmuO-Co^{III} and Myo-Co^{III} gave comparable TONs but the former was much more selective for CO. Using Cu-PS as the photosensitizer and identical reaction conditions, for a more relevant comparison, we show here that HmuO-Co^{III} gave slightly higher TON and selectivity.

In conclusion, the HmuO-Co^{III}-dependent system provides a unique platform for exploring the reactivity of an ACR. Further structural and mutagenesis studies should be carried out and other photosensitizers should be evaluated since this field continues to suffer from an excessive instability of current organic dyes and organometallic complexes.

Supplementary information. The atomic coordinates and structures factors for HmuO-Co^{III}, HmuO-Co^{III}-CO$_2$, HmuO-H20C, HmuO-G139A and HmuO-I143K obtained in this work are deposited in the Protein Data Bank, under accession codes: 9F5U, 9F66, 9FW4, 9FVS and 9FY4 respectively. Tables and Figures explaining more extensively the results reported in this article and additional figures presenting structural and photocatalytic investigation are found in the Supplementary Material.

Notes. The authors declare no competing financial interest.

References.

1.	Grim, R. G.; Ferrell, J. I. I. I.; Huang, Z.; Tao, L.; Resch, M. G., The feasibility of direct CO_2 conversion technologies on impacting mid-century climate goals. *Joule* **2023,** *7* (8), 1684-1699.
2.	She, X. J.; Wang, Y. F.; Xu, H.; Tsang, S. C. E.; Lau, S. P., Challenges and Opportunities in Electrocatalytic CO_2 Reduction to Chemicals and Fuels. *Angew Chem Int Edit* **2022,** *61* (49).
3.	Yang, Z. W.; Chen, J. M.; Qiu, L. Q.; Xie, W. J.; He, L. N., Molecular Engineering of Metal Complexes for Electrocatalytic Carbon Dioxide Reduction: From Adjustment of Intrinsic Activity to Molecular Immobilization. *Angew Chem Int Edit* **2022,** *61* (44).
4.	Kinzel, N. W.; Werlé, C.; Leitner, W., Transition Metal Complexes as Catalysts for the Electroconversion of CO_2 : An Organometallic Perspective. *Angew Chem Int Edit* **2021,** *60* (21), 11628-11686.
5.	Zhang, X. L.; Guo, S. X.; Gandionco, K. A.; Bond, A. M.; Zhang, J., Electrocatalytic carbon dioxide reduction: from fundamental principles to catalyst design. *Mater Today Adv* **2020,** *7*.
6.	Stripp, S. T.; Duffus, B. R.; Fourmond, V.; Leger, C.; Leimkuhler, S.; Hirota, S.; Hu, Y.; Jasniewski, A.; Ogata, H.; Ribbe, M. W., Second and Outer Coordination Sphere Effects in Nitrogenase, Hydrogenase, Formate Dehydrogenase, and CO Dehydrogenase. *Chem Rev* **2022,** *122* (14), 11900-11973.
7.	Appel, A. M.; Bercaw, J. E.; Bocarsly, A. B.; Dobbek, H.; DuBois, D. L.; Dupuis, M.; Ferry, J. G.; Fujita, E.; Hille, R.; Kenis, P. J. A.; Kerfeld, C. A.; Morris, R. H.; Peden, C. H. F.; Portis, A. R.; Ragsdale, S. W.; Rauchfuss, T. B.; Reek, J. N. H.; Seefeldt, L. C.; Thauer, R. K.; Waldrop, G. L., Frontiers, Opportunities, and Challenges in Biochemical and Chemical Catalysis of CO_2 Fixation. *Chem Rev* **2013,** *113* (8), 6621-6658.
8.	Schwizer, F.; Okamoto, Y.; Heinisch, T.; Gu, Y. F.; Pellizzoni, M. M.; Lebrun, V.; Reuter, R.; Köhler, V.; Lewis, J. C.; Ward, T. R., Artificial Metalloenzymes: Reaction Scope and Optimization Strategies. *Chem Rev* **2018,** *118* (1), 142-231.
9.	Waser, V.; Mukherjee, M.; Igareta, N. V.; Tachibana, R.; Ward, T. R., An Artificial [4Fe-4S]-Containing Metalloenzyme for the Reduction of CO_2 to Hydrocarbons. *J Am Chem Soc* **2023,** *145* (27), 14823-14830.
10.	Yokoi, N.; Miura, Y.; Huang, C. Y.; Takatani, N.; Inaba, H.; Koshiyama, T.; Kanamaru, S.; Arisaka, F.; Watanabe, Y.; Kitagawa, S.; Ueno, T., Dual modification of a triple-stranded β-helix nanotube with Ru and Re metal complexes to promote photocatalytic reduction of CO_2. *Chem Commun* **2011,** *47* (7), 2074-2076.
11.	Schneider, C. R.; Shafaat, H. S., An internal electron reservoir enhances catalytic CO_2 reduction by a semisynthetic enzyme. *Chem Commun* **2016,** *52* (64), 9889-9892.
12.	Schneider, C. R.; Manesis, A. C.; Stevenson, M. J.; Shafaat, H. S., A photoactive semisynthetic metalloenzyme exhibits complete selectivity for CO_2 reduction in water. *Chem Commun* **2018,** *54* (37), 4681-4684.
13.	Liu, X. H.; Kang, F. Y.; Hu, C.; Wang, L.; Xu, Z.; Zheng, D. D.; Gong, W. M.; Lu, Y.; Ma, Y. H.; Wang, J. Y., A genetically encoded photosensitizer protein facilitates the rational design of a miniature photocatalytic CO_2-reducing enzyme. *Nature Chemistry* **2018,** *10* (12), 1201-1206.
14.	Kang, F. Y.; Yu, L.; Xia, Y.; Yu, M. L.; Xia, L.; Wang, Y. C. A.; Yang, L.; Wang, T. Y.; Gong, W. M.; Tian, C. L.; Liu, X. H.; Wang, J. Y., Rational Design of a Miniature Photocatalytic CO_2-Reducing Enzyme. *Acs Catal* **2021,** *11* (9), 5628-5635.
15.	Terholsen, H.; Huerta-Zerón, H. D.; Möller, C.; Junge, H.; Beller, M.; Bornscheuer, U. T., Photocatalytic CO_2 Reduction Using CO_2-Binding Enzymes. *Angew Chem Int Edit* **2024,** *63* (16).
16.	Deng, Y. L.; Dwaraknath, S.; Ouyang, W. O.; Matsumoto, C. J.; Ouchida, S.; Lu, Y., Engineering an Oxygen-Binding Protein for Photocatalytic CO_2 Reductions in Water. *Angew Chem Int Edit* **2023,** *62* (20).
17.	Udry, G. A. O.; Tiessler-Sala, L.; Pugliese, E.; Urvoas, A.; Halime, Z.; Maréchal, J. D.; Mahy, J. P.; Ricoux, R., Photocatalytic Hydrogen Production and Carbon Dioxide Reduction Catalyzed by an Artificial Cobalt Hemoprotein. *Int J Mol Sci* **2022,** *23* (23).
18.	Manbeck, G. F.; Fujita, E., A review of iron and cobalt porphyrins, phthalocyanines and related complexes for electrochemical and photochemical reduction of carbon dioxide. *J Porphyr Phthalocya* **2015,** *19* (1-3), 45-64.

19.   Call, A.; Cibian, M.; Yamamoto, K.; Nakazono, T.; Yamauchi, K.; Sakai, K., Highly Efficient and Selective Photocatalytic CO_2 Reduction to CO in Water by a Cobalt Porphyrin Molecular Catalyst. *Acs Catal* **2019,** *9* (6), 4867-4874.

20.   Zhang, X.; Cibian, M.; Call, A.; Yamauchi, K.; Sakai, K., Photochemical CO_2 Reduction Driven by Water-Soluble Copper(I) Photosensitizer with the Catalysis Accelerated by Multi-Electron Chargeable Cobalt Porphyrin. *Acs Catal* **2019,** *9* (12), 11263-11273.

21.   Shen, J.; Kortlever, R.; Kas, R.; Birdja, Y. Y.; Diaz-Morales, O.; Kwon, Y.; Ledezma-Yanez, I.; Schouten, K. J. P.; Mul, G.; Koper, M. T. M., Electrocatalytic reduction of carbon dioxide to carbon monoxide and methane at an immobilized cobalt protoporphyrin. *Nature Communications* **2015,** *6*.

22.   Hu, X. M.; Ronne, M. H.; Pedersen, S. U.; Skrydstrup, T.; Daasbjerg, K., Enhanced Catalytic Activity of Cobalt Porphyrin in CO_2 Electroreduction upon Immobilization on Carbon Materials. *Angew Chem Int Edit* **2017,** *56* (23), 6468-6472.

23.   Zhu, M. H.; Chen, J. C.; Huang, L. B.; Ye, R. Q.; Xu, J.; Han, Y. F., Covalently Grafting Cobalt Porphyrin onto Carbon Nanotubes for Efficient CO_2 Electroreduction. *Angew Chem Int Edit* **2019,** *58* (20), 6595-6599.

24.   Kim, Y. H.; Jeon, J. P.; Kim, Y.; Noh, H. J.; Seo, J. M.; Kim, J.; Lee, G.; Baek, J. B., Cobalt-Porphyrin-Based Covalent Organic Frameworks with Donor-Acceptor Units as Photocatalysts for Carbon Dioxide Reduction. *Angew Chem Int Edit* **2023,** *62* (36).

25.   Sudhamsu, J.; Kabir, M.; Airola, M. V.; Patel, B. A.; Yeh, S. R.; Rousseau, D. L.; Crane, B. R., Co-expression of ferrochelatase allows for complete heme incorporation into recombinant proteins produced in E. coli. *Protein Expres Purif* **2010,** *73* (1), 78-82.

26.   Honda, Y.; Nanasawa, K.; Fujii, H., Coexpression of 5-Aminolevulinic Acid Synthase Gene Facilitates Heterologous Production of Thermostable Cytochrome P450, CYP119, in Holo Form in Escherichia coli. *Chembiochem* **2018,** *19* (20), 2156-2159.

27.   Sreenilayam, G.; Moore, E. J.; Steck, V.; Fasan, R., Metal Substitution Modulates the Reactivity and Extends the Reaction Scope of Myoglobin Carbene Transfer Catalysts. *Adv Synth Catal* **2017,** *359* (12), 2076-2089.

28.   Yonetani, T.; Yamamoto, H.; Woodrow, G. V., Studies on Cobalt Myoglobins and Hemoglobins .1. Preparation and Optical-Properties of Myoglobins and Hemoglobins Containing Cobalt Proto-Porphyrins, Meso-Porphyrins, and Deuteroporphyrins and Thermodynamic Characterization of Their Reversible Oxygenation. *J Biol Chem* **1974,** *249* (3), 682-690.

29.   Cai, Y. B.; Yao, S. Y.; Hu, M.; Liu, X. Y.; Zhang, J. L., Manganese protoporphyrin IX reconstituted myoglobin capable of epoxidation of the C=C bond with Oxone®. *Inorg Chem Front* **2016,** *3* (10), 1236-1244.

30.   Srivastava, T. S., Chromium (III) Myoglobin. *Curr Sci India* **1979,** *48* (9), 391-393.

31.   Yamada, T.; Morita, Y.; Takada, R.; Funamoto, M.; Okamoto, W.; Kohno, M.; Komatsu, T., Zinc Substituted Myoglobin-Albumin Fusion Protein: A Photosensitizer for Cancer Therapy. *Chem-Eur J* **2023,** *29* (22).

32.   Hirotsu, S.; Chu, G. C.; Unno, M.; Lee, D. S.; Yoshida, T.; Park, S. Y.; Shiro, Y.; Ikeda-Saito, M., The Crystal Structures of the Ferric and Ferrous Forms of the Heme Complex of HmuO, a Heme Oxygenase of Corynebacterium diphtheriae*. *J Biol Chem* **2004,** *279* (12), 11937-11947.

33.   von Stetten, D.; Giraud, T.; Carpentier, P.; Sever, F.; Terrien, M.; Dobias, F.; Juers, D. H.; Flot, D.; Mueller-Dieckmann, C.; Leonard, G. A.; de Sanctis, D.; Royant, A., In crystallo optical spectroscopy (icOS) as a complementary tool on the macromolecular crystallography beamlines of the ESRF. *Acta Crystallogr D* **2015,** *71*, 15-26.

34.   Kim, J. K.; Cho, Y. S.; Lee, M.; Laskowski, R. A.; Ryu, S. E.; Sugihara, K.; Kim, D. S., BetaCavityWeb: a webserver for molecular voids and channels. *Nucleic Acids Res* **2015,** *43* (W1), W413-W418.

35.   Matsui, T.; Furukawa, M.; Unno, M.; Tomita, T.; Ikeda-Saito, M., Roles of distal Asp in heme oxygenase from Corynebacterium diphtheriae, HmuO: A water-driven oxygen activation mechanism. *J Biol Chem* **2005,** *280* (4), 2981-2989.

36.   Matsui, T.; Iwasaki, M.; Sugiyama, R.; Unno, M.; Ikeda-Saito, M., Dioxygen Activation for the Self-Degradation of Heme: Reaction Mechanism and Regulation of Heme Oxygenase. *Inorg Chem* **2010,** *49* (8), 3602-3609.

37.   Lafumat, B.; Mueller-Dieckmann, C.; Leonard, G.; Colloc'h, N.; Prangé, T.; Giraud, T.; Dobias, F.; Royant, A.; van der Linden, P.; Carpentier, P., Gas-sensitive biological crystals processed in pressurized oxygen and krypton atmospheres: deciphering gas channels in proteins using a novel 'soak-and-freeze' methodology. *J Appl Crystallogr* **2016,** *49*, 1478-1487.

38.   Carpentier, P.; van der Linden, P.; Mueller-Dieckmann, C., The High-Pressure Freezing Laboratory for Macromolecular Crystallography (HPMX), an ancillary tool for the macromolecular crystallography beamlines at the ESRF. *Acta Crystallogr D* **2024,** *80*, 80-92.

39.   Carpentier, P.; Royant, A.; Ohana, J.; Bourgeois, D., Advances in spectroscopic methods for biological crystals. 2. Raman spectroscopy. *J Appl Crystallogr* **2007,** *40*, 1113-1122.

40.   De Gelder, J.; De Gussem, K.; Vandenabeele, P.; Moens, L., Reference database of Raman spectra of biological molecules. *J Raman Spectrosc* **2007,** *38* (9), 1133-1147.

41.   Fermi, E., Über den ramaneffekt des kohlendioxyds. **1931,** *71* (3), 250-259.

42.   Lehn, J. M.; Ziessel, R., Photochemical Reduction of Carbon-Dioxide to Formate Catalyzed by 2,2'-Bipyridine-Ruthenium(Ii) or 1,10-Phenanthroline-Ruthenium(Ii) Complexes. *J Organomet Chem* **1990,** *382* (1-2), 157-173.

43.   Poulos, T. L.; Finzel, B. C.; Howard, A. J., High-Resolution Crystal-Structure of Cytochrome-P450cam. *J Mol Biol* **1987,** *195* (3), 687-700.

44.   Gouet, P.; Jouve, H. M.; Williams, P. A.; Andersson, I.; Andreoletti, P.; Nussaume, L.; Hajdu, J., Ferryl intermediates of catalase captured by time-resolved Weissenberg crystallography and UV-VIS spectroscopy. *Nat Struct Biol* **1996,** *3* (11), 951-956.

45.   Perkins, L. J.; Weaver, B. R.; Buller, A. R.; Burstyn, J. N., De novo biosynthesis of a nonnatural cobalt porphyrin cofactor in E. coli and incorporation into hemoproteins. *P Natl Acad Sci USA* **2021,** *118* (16).

46.   Wang, J. W.; Zhang, X.; Velasco, L.; Karnahl, M.; Li, Z. Z.; Luo, Z. M.; Huang, Y. J.; Yu, J.; Hu, W. H.; Zhang, X. Y.; Yamauchi, K.; Sakai, K.; Moonshiram, D.; Ouyang, G. F., Precious-Metal-Free CO_2 Photoreduction Boosted by Dynamic Coordinative Interaction between Pyridine-Tethered Cu(I) Sensitizers and a Co(II) Catalyst. *Jacs Au* **2023,** *3* (7), 1984-1997.

47.   Shen, J.; Kolb, M. J.; Göttle, A. J.; Koper, M. T. M., DFT Study on the Mechanism of the Electrochemical Reduction of CO_2 Catalyzed by Cobalt Porphyrins. *J Phys Chem C* **2016,** *120* (29), 15714-15721.

48.   Labidi, R. J.; Faivre, B.; Carpentier, P.; Veronesi, G.; Solé-Daura, A.; Bjornsson, R.; Léger, C.; Gotico, P.; Li, Y.; Atta, M.; Fontecave, M., Light-Driven Hydrogen Evolution Reaction Catalyzed by a Molybdenum-Copper Artificial Hydrogenase. *J Am Chem Soc* **2023,** *145* (25), 13640-13649.

49.   Alcala-Torano, R.; Halloran, N.; Gwerder, N.; Sommer, D. J.; Ghirlanda, G., Light-Driven CO_2 Reduction by Co-Cytochrome b562. *Front Mol Biosci* **2021,** *8*.
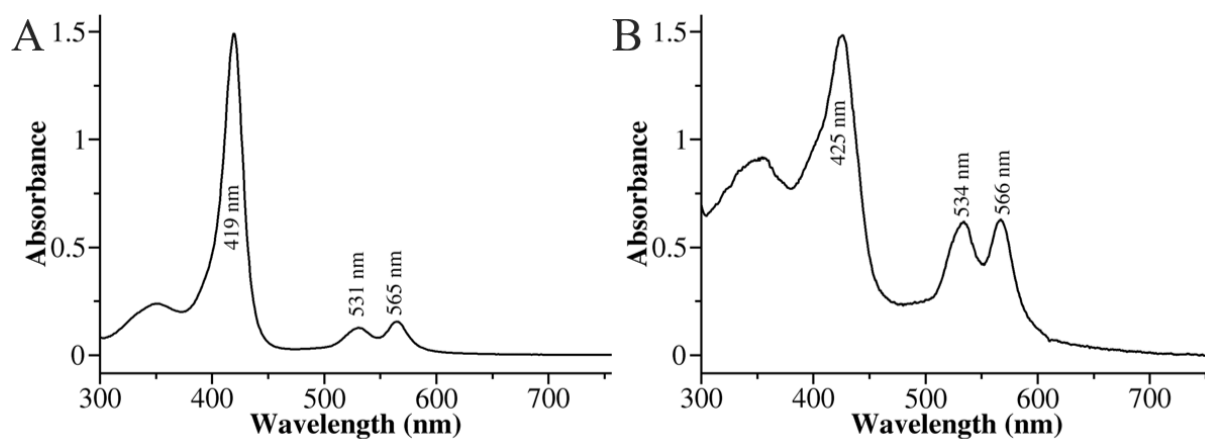
Figure 1.

Figure 1. UV–visible spectroscopy of HmuO-Co^{III}. (A) Spectrum was recorded with 10.3 µM of HmuO-Co^{III} solution in 100 mM phosphate pH 7. The concentrations of proteins was estimated by Bradford assay using bovine albumin as standard. (B) Spectrum *in crystallo* recorded in HmuO-Co^{III} crystal measured at the iCOS laboratory (ESRF, Grenoble).
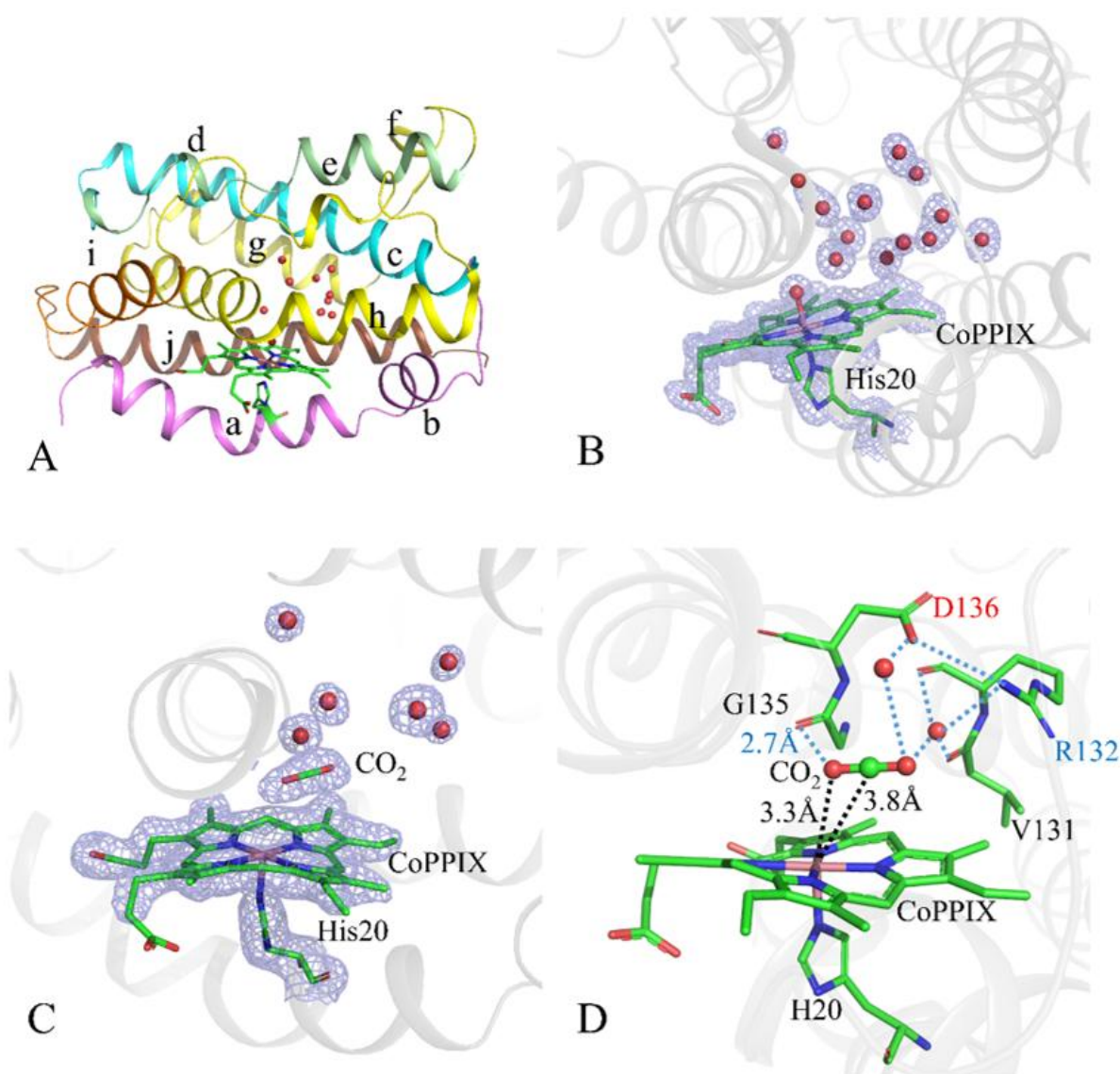
Figure 2.

Figure 2. Structures of HmuO-Co^{III} and HmuO-Co^{III}-CO$_2$. (A) Overall structure of HmuO-Co^{III}, represented as a ribbon. The different helices are colored and labeled (from a to j) as previously defined[32]. In particular, the proximal and distal helices are shown in magenta (b) and yellow (h), respectively. The cobalt-protoporphyrin IX cofactor bound to HmuO is shown in stick (green) and water molecules are shown as red spheres. (B) A close-up view the 2Fo-Fc electron density maps (blue mesh) contoured at 1σ around the cobalt-protoporphyrin IX cofactor and the water molecules. (C) Close-up view of the active site with 2Fo-Fc electron density maps contoured at 1σ (blue mesh) of the HmuO-Co^{III}-CO$_2$ structure obtained from a crystal pressurized with 58 bar of CO$_2$. A CO$_2$ molecule was suitably modeled in the electron density in the distal cavity. (D) Representation of the CO$_2$ environment in the distal cavity of HmO-Co^{III}-CO$_2$. Hydrogen bonds network are shown as blue dotted lines, extended from cobalt to D136 at the protein surface. Red spheres represent the two water molecules involved in the interaction with CO$_2$.
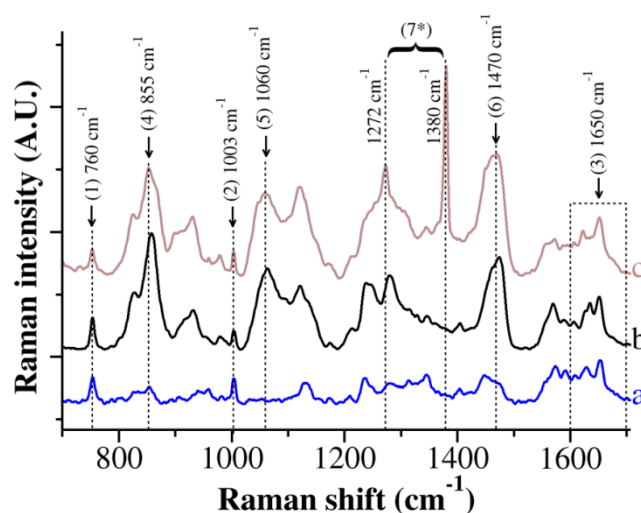
Figure 3.

Figure 3. Raman spectra of HmuO-Co^{III} crystals. Spectra were recorded at 100 K for with a 785 nm laser at the icOS laboratory (ESRF, Grenoble). (a,b) Raman spectrum of HmuO-Co^{III} crystal frozen in its crystallization solution without glycerol (a) and with glycerol (b) as cryoprotectant (black). The Raman bands (1), (2) and (3) correspond to vibration of tryptophan (760 cm^{-1}), phenylalanine (1005 cm^{-1}) and amide I (1650 cm^{-1}) respectively of the HmuO-Co^{III} protein. (4), (5) and (6) Raman bands attributed to the glycerol molecule. (c) Raman spectrum of HmuO-Co^{III}-CO$_2$ frozen with glycerol, which was used for the X-ray data collection. The Raman doublet-band (7*) corresponds to the Fermi dyad of CO$_2$ peaking at 1272cm^{-1} and 1380cm^{-1}, which confirms the presence of CO$_2$ in the crystal.
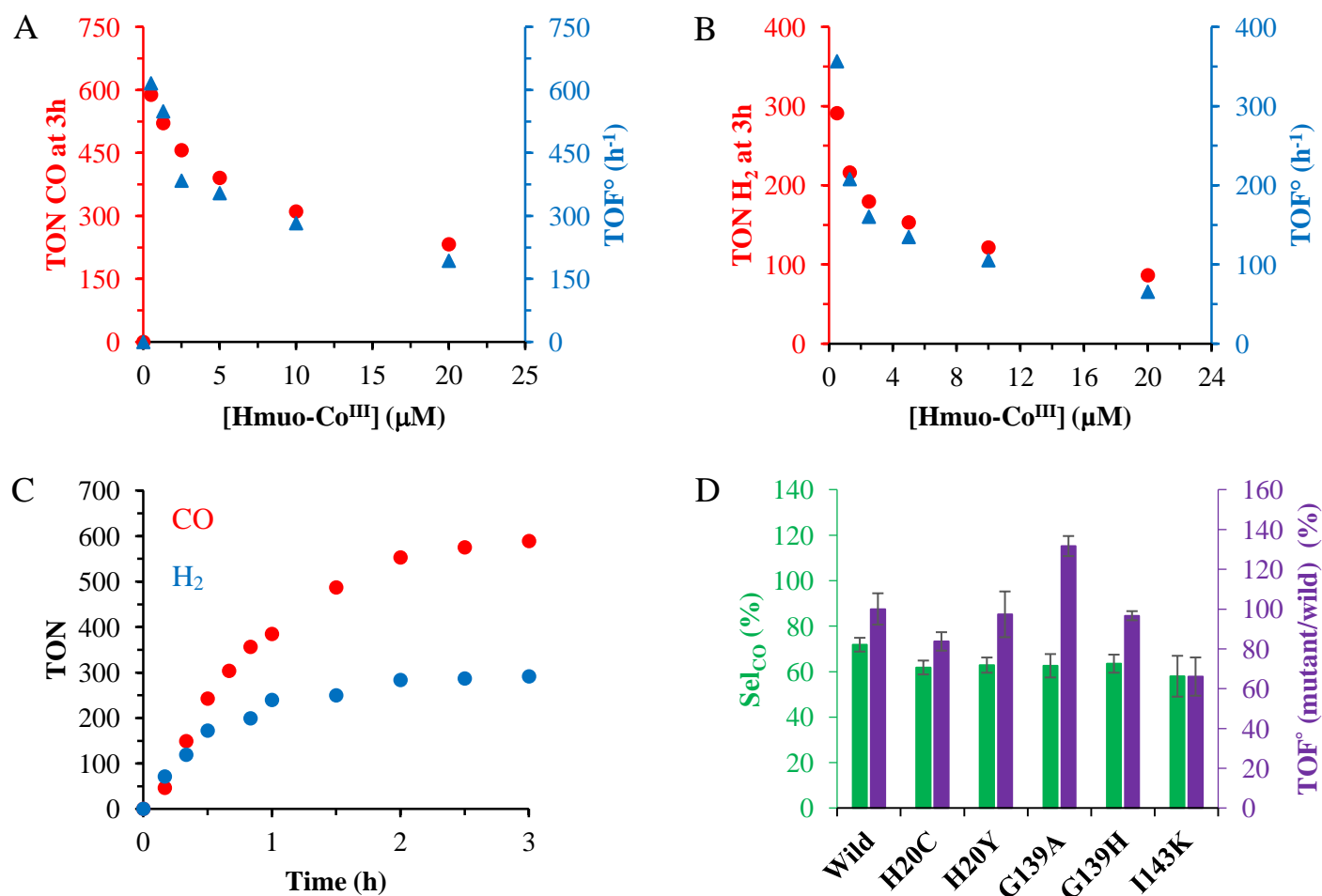
Figure 4.

Figure 4. Photocatalytic activity of HmuO-Co^{III} and mutants on CO and H$_2$ production. CO (A) and H$_2$ (B) production as a function of the concentration of HmuO-Co^{III} after 3h of irradiation (red dots) and maximum rates determined from the first 20 minutes of irradiation (blue triangles). (C) Optimal photocatalytic CO and H$_2$ production using the HmuO-Co^{III}/Cu-PS/L-AscHNa system. (D) Selectivities for CO$_2$ reduction (Sel_{CO_2} (%) = $TOF_{CO}°$/ [$TOF_{CO}°$+ $TOF_{H_2}°$]) (green bars) and relative TOF°$_{CO}$ of the protein derivatives with respect to the TOF°$_{CO}$ of the wild type protein (purple bars). Data represent mean values from triplicates. Experimental conditions: photocatalysis was carried out in a 2 ml CO$_2$-saturated solution with 0.5-20 μM HmuO-Co^{III} (A and B), 0.5 μM HmuO-Co^{III} (C), 1.3 μM (D) containing 1 mM Cu-PS, 100 mM L-AscHNa, 0.5 M potassium phosphate buffer (pH 6.65), T = 20 °C, using Xe lamp irradiation (> 400 nm).
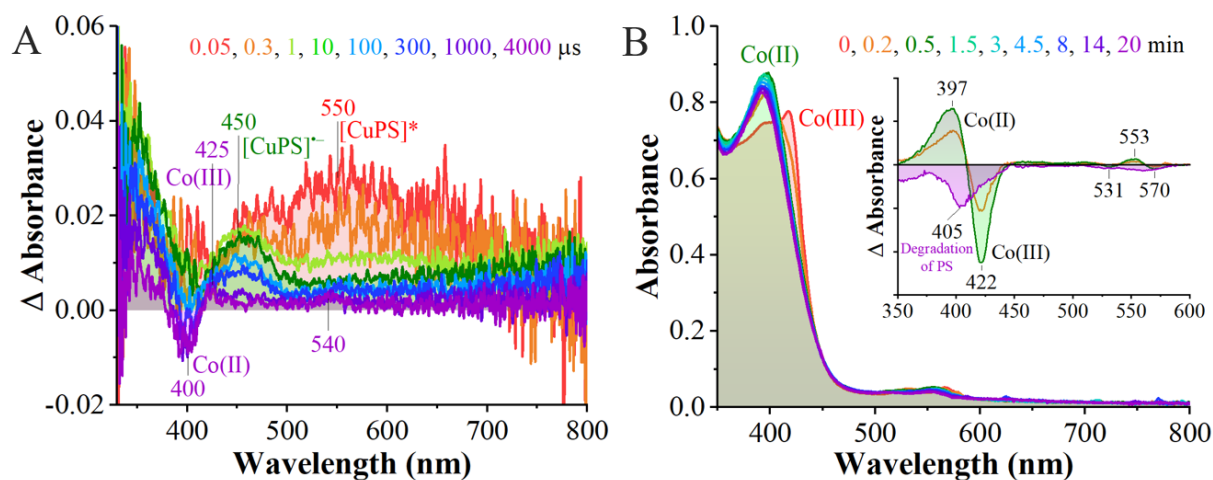
Figure 5

Figure 5. Spectral tracking of intermediates. (a) Transient absorption spectroscopy of 95 μM Cu-PS with 33 mM Asc and 7 µM HmuO-Co^{III} catalyst in Ar-saturated phosphate buffer (pH 7) at different time delays (λ_{exc} = 420 nm, E = 8 mJ). (b) *In situ* spectroscopy of 173 µM Cu-PS with 43 mM Asc and 2.5 µM HmuO-Co^{III} catalyst in CO$_2$-saturated phosphate buffer at different time delays (white LED irradiation, 200 W m^{-2}). Inset shows the differential absorption for the orange, green and violet traces.
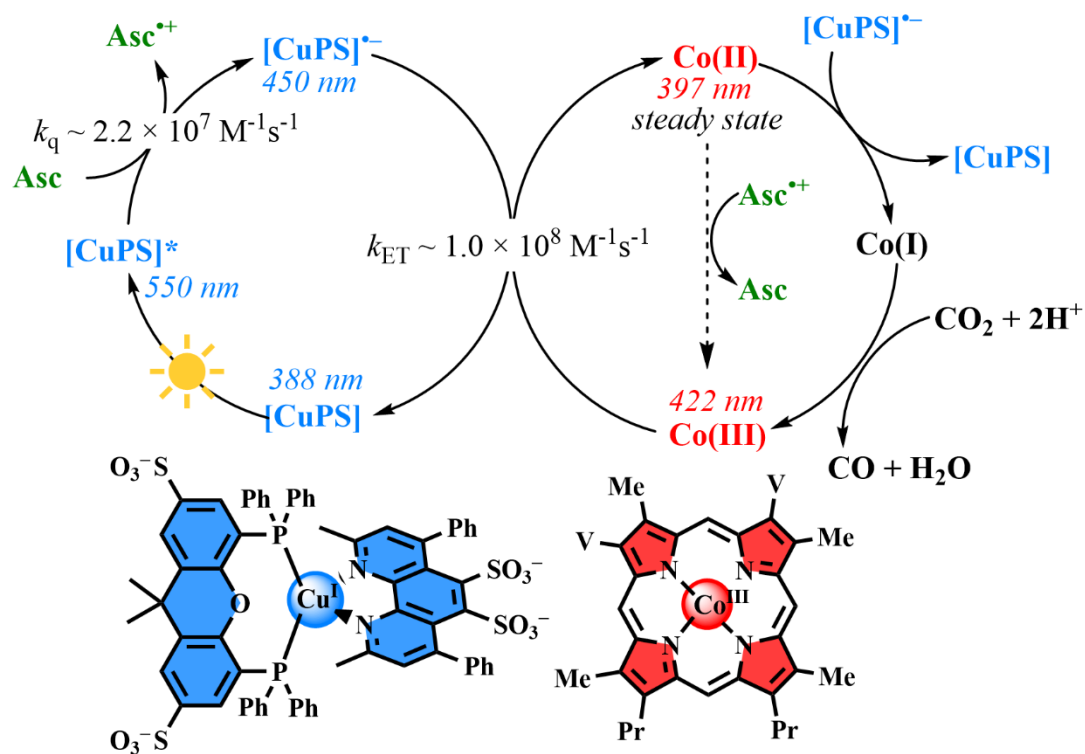
Figure 6

Figure 6. Proposed photocatalytic cycle for the photo-induced activity of artificial CO$_2$ reductase based on HmuO-CO^{III}/Cu-PS/Asc system. All colored intermediates were spectrally tracked in the study while intermediates in black are not followed but hypothesized to occur based on previous studies.[46-47]

ToC graphic.